OPEN ACCESS
IOP Publishing
Journal of Physics D: Applied Physics
J. Phys. D: Appl. Phys. **55** (2022) 285302 (13pp)
https://doi.org/10.1088/1361-6463/ac6466

Frequency-controlled dielectrophoresis-driven wetting of nematic liquid crystals

Carl V Brown[1,*], Akhshay S Bhadwal[1], Andrew M J Edwards[1], Ian C Sage[1], Antariksh Saxena[1] and Nigel J Mottram[2]

[1] SOFT Group, School of Science and Technology, Nottingham Trent University, Clifton Lane, Nottingham NG11 8NS, United Kingdom
[2] School of Mathematics and Statistics, University of Glasgow, University Place, Glasgow G12 8QQ, United Kingdom

E-mail: carl.brown@ntu.ac.uk

Received 4 February 2022, revised 20 March 2022
Accepted for publication 5 April 2022
Published 22 April 2022

Abstract

We show that surface-localized dielectrophoresis-driven wetting of anisotropic nematic liquid crystal sessile droplets obeys the same relationship, $\cos[\theta(V_o)] = \cos[\theta_Y] - \beta V_o^2$, which has previously been found for isotropic liquid droplets, even though the nematic liquid crystal phase possesses a uniaxial dielectric permittivity tensor. We also demonstrate that the dielectrowetting coefficient β, which determines the magnitude of the reduction in the contact angle, from θ_Y to $\theta(V_o)$, through the action of a potential difference V_o, can be controlled by the frequency of the applied voltage between interdigitated electrodes beneath a droplet of highly dispersive nematic liquid crystal. Our Q-tensor modelling of the electric field-induced 2-dimensional n-director distortions within a nematic droplet elucidates how this linear relationship holds for voltages when $|\theta(V_o) - \theta_Y|$ exceeds 3°–4°.

Keywords: dielectrophoresis, nematic liquid crystals, wetting, droplets

(Some figures may appear in colour only in the online journal)

1. Introduction

Dielectrophoresis, in general, refers to the force exerted on an electrically neutral polarisable dielectric material when it is subjected to a non-uniform electric field [1]. The dielectrophoretic manipulation of the trajectories of polarisable particles using spatially inhomogeneous electric fields has been exploited in applications ranging from biomedical lab-on-a-chip and microfluidic technologies such as diagnostics and cell-based therapies [2, 3] to field flow fractionation for selective separation and classification of particles [4, 5]. In liquid dielectrophoresis, the material used is typically an electrically insulating liquid. The classic experimental demonstration of this effect is Pellat's height-of-rise experiment [6–8]. Dielectrophoresis-induced bulk liquid movement minimises the energy of the system when the high dielectric constant liquid replaces the low dielectric constant air in the region of maximum electric field between two capacitor plates that are at a potential difference [9]. Electrical actuation of liquids and droplets via liquid dielectrophoresis has been exploited in applications including wall-less microfluidic and droplet dispensing devices [7] and in optofluidic devices such as tuneable liquid lenses, shutters, and beamsteerers [10, 11].

Surface-localised dielectrophoretic actuation of liquids has been achieved via co-planar and interdigitated electrodes that are embedded into a solid surface. The highly non-uniform electric fields produced by the electrode array penetrate a short

* Author to whom any correspondence should be addressed.

Original content from this work may be used under the terms of the Creative Commons Attribution 4.0 licence. Any further distribution of this work must maintain attribution to the author(s) and the title of the work, journal citation and DOI.

© 2022 The Author(s). Published by IOP Publishing Ltd

distance into the liquid and polarise the molecular dipoles in the liquid adjacent to the surface. The balance between the interfacial energies and the electrostatic energy in the system compels the dielectric liquid to move across or spread down onto, the surface [7, 12, 13]. Applications include digital droplet microfluidics [14], switchable diffractive beamsteering [15] and lenses with voltage adjustable focal length [16]. In 'dielectrowetting' this surface-localised dielectrophoresis effect has been used to force an electrically insulating isotropic liquid to wet down onto a normally liquid repellent surface and create a fully spread liquid film [17]. It has been shown that the difference between the cosines of the quasistatic and the zero-field contact angles of the liquid, $\theta(V_o)$ and θ_Y (viewed orthogonal to the spreading direction), is directly proportional to the square of the voltage potential difference V_o applied between adjacent electrodes in the interdigitated array [17]. This dielectrowetting relationship has been found to hold for a range of different isotropic electrically insulating liquids, both in air and immersed in other immiscible liquids [18].

Nematic liquid crystal materials have very attractive properties for optofluidic devices based on dielectrophoretic actuation because these materials are manufactured with high purity and low electrical conductivity for the display industry, and they are designed to have high dielectric constants and so they are highly polarisable [19]. Examples of such devices utilising nematic liquids include a reconfigurable lens with a circular interdigitated electrode geometry [16] and a voltage-expandable liquid crystal droplet or film controlled by an interdigitated electrode array to provide a programmable optical shutter or coloured filter function [20–23]. In these systems, commercial nematic liquid crystals with positive dielectric anisotropy were used for which the magnitude of the largest permittivity, measured parallel to the nematic *n*-director $\varepsilon_{\parallel}$, was in the range 16.5–56.0, including the specified materials MDA2625, ZLI4389, and MLC2140 from Merck KGaA, Darmstadt, Germany. In these applications there is an interface between the nematic material and another, less polarisable, immiscible liquid. The voltage actuation is achieved by dielectrophoresis induced movement of the contact line between the two liquids across the solid surface which brings more of the higher dielectric permittivity nematic liquid crystal material into the vicinity of the strongest electric fields produced by the electrodes. Within the nematic liquid crystal that lies above the interdigitated electrodes the non-uniform electric fields couple to the uniaxial anisotropic polarisability of the adjacent nematic liquid crystal material, which produces voltage-induced reorientation and surface localised distortion of the *n*-director field. In fully confined systems, the resultant electro-optic switching effect has been studied in detail and exploited for wide viewing angle Vertically-Aligned In-Plane Switch VA-IPS displays [24–31].

In this report, we present a detailed investigation of the dielectrowetting of unconfined sessile nematic liquid crystal droplets in the air using surface-localised dielectrophoresis. In section 3.1 we provide an experimental demonstration that two different nematic materials obey the $(\cos[\theta(V_o)] - \cos[\theta_Y]) = \beta V_o^2$ dielectrowetting relationship. In section 3.2 we use Q-tensor modelling to elucidate the consequences of the *n*-director reorientation that also occurs due to the action of the highly non-uniform electric fields produced by the actuating electrodes. Finally, in section 3.3, we consequently demonstrate the possibility of tailoring the extent of dielectrowetting not only through control of the voltage amplitude but also through a novel frequency dependence of the dielectrowetting constant β in a highly dispersive nematic liquid crystal material.

2. Experimental methods

Figure 1(a) shows a schematic diagram of a sessile nematic liquid crystal droplet resting on a solid device substrate. The substrate lies in the *x*-*y* plane and carries an interdigitated electrode micro-stripe array, as shown in figure 1(b), overcoated with the amorphous fluorinated dielectric polymer Teflon AF. The device was fabricated from a glass substrate coated with transparent conducting electrodes (Indium Tin Oxide, 25 nm thickness and 100 Ohm per square resistivity, Praezisions Glass and Optick GmbH, Germany). We used standard photolithographic and etching techniques to pattern the indium tin oxide coating to produce interdigitated electrodes arranged in a linear co-planar micro-stripe array covering a rectangular area $L_x = 10$ mm $\times$ $L_y = 2$ mm, with the stripes parallel to the *x*-direction. The electrode line widths, as well as the gaps between adjacent electrodes, were both given by $w = 20$ μm. The electrodes were capped with a protective planarizing dielectric layer of SU-8 photoresist (Microchem Corp., thickness 1 μm). The resultant structure was over-coated with the amorphous fluorinated copolymer Teflon AF (poly[4,5-difluoro-2,2-bis(trifluoromethyl)-1,3-dioxole-co-tetrafluoroethylene], 'PTFE AF 2400', dioxole 87 mol%, CAS 37 626-13-4, Sigma-Aldrich/Merck KGaA, Darmstadt, Germany). The over-coating was deposited from a solution of Teflon AF made up in its solvent, Octadecafluorodecahydronaphthalene (CAS numbers 37 626-13-4 and 306-94-5, Sigma-Aldrich/Merck KGaA, Darmstadt, Germany), at 0.75% by weight. This solution was dip-coated onto the substrate, which was then dried at room temperature for 5 min and baked at 60 °C for 10 min.

The nematic liquid crystal materials E7 and MLC2048 used in our study are both well-characterised materials for which all three elastic constants are available. E7 is a eutectic mixture consisting of four cyano substituted polyphenyl components [32, 33]. The elastic constants of E7 are $K_1 = 11.2$ pN, $K_2 = 6.8$ pN, and $K_3 = 18.6$ pN [34, 35]. The permittivities parallel and the perpendicular to the nematic *n*-director for E7 are $\varepsilon_{\parallel} = 18.96$ and $\varepsilon_{\perp} = 5.16$, respectively, with $\Delta\varepsilon = \varepsilon_{\parallel} - \varepsilon_{\perp} = 13.80$, and these values do not vary significantly with A.C. excitation voltage frequency over the 1 kHz to 100 kHz range [34, 35]. MLC2048 (Merck KGaA, Darmstadt, Germany) is a highly dispersive nematic material, also known as a 'dual-frequency' or '2 *f*' material, in which there is a low-frequency relaxation of the magnitude of the permittivity measured parallel to the nematic *n*-director, $\varepsilon_{\parallel}$ [36, 37].

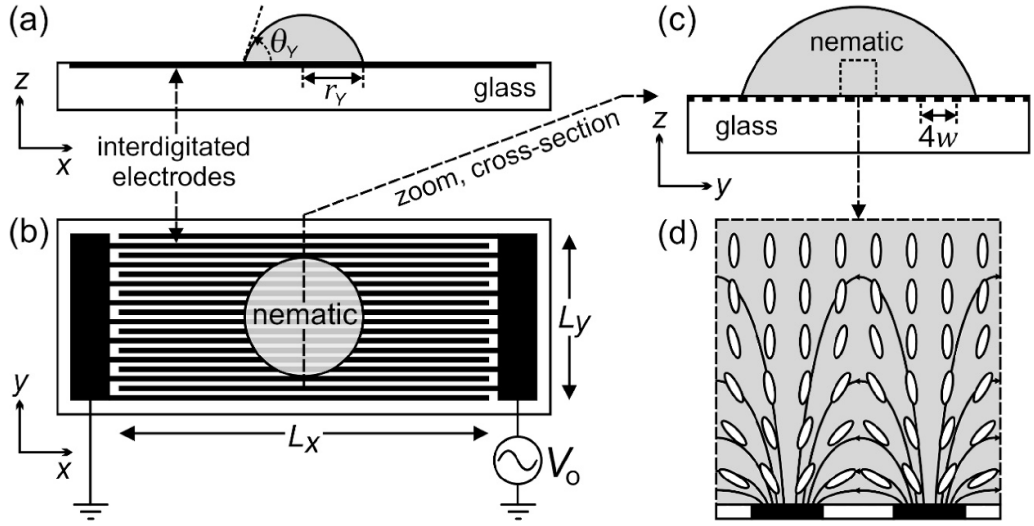

Figure 1. Schematic diagrams of a nematic liquid crystal droplet, with equilibrium contact angle θ_Y and base radius r_Y, resting on a solid substrate in the x-y plane on which there was an interdigitated electrode micro-stripe array overcoated with Teflon AF. A side view from along the y-direction and a top view from along the z-direction are shown in (a) and (b), respectively. (c) shows a y-z cross-section through the droplet, electrodes, and substrate, within which (d) shows an expanded view of an 80 μm × 80 μm region within the droplet when $V_o \neq 0$. In (d) the solid lines depict electric fields, and the open ellipses depict the local orientation of the nematic n-director for a positive dielectric anisotropy material.

The relaxation is of sufficient magnitude that the dielectric anisotropy changes sign in the kHz frequency range, and the resultant frequency dependent switching capability has been exploited in fully confined geometries including displays and optofluidic devices [38, 39]. Hence, the material MLC2048 was chosen for the present study because of its previous use in electrically tuneable lenses applications [38] and because the material's low frequency relaxation permits our study of dielectrowetting in an experimentally accessible frequency range of 1 kHz to 30 kHz. This frequency range avoids low frequency ionic free charge shielding effects and also avoids high frequency voltage signal losses due to the finite conductivity of the indium tin oxide electrodes. The elastic constants of MLC2048, which are not frequency dependent, are $K_1 = 15.4$ pN, $K_2 = 12.6$ pN, and $K_3 = 21.5$ pN [40, 41].

We measured the dielectric permittivities $\varepsilon_{\parallel}$ and $\varepsilon_{\perp}$ for MLC2048 using an Agilent 4284A LCR meter with an A.C. excitation voltage of 0.1 $V_{R.M.S.}$ over a range of frequencies f from 1 kHz to 30 kHz. The measurement was performed with the material contained in commercial capacitance test cells that consisted of a continuous electrode on one plate opposed by a circular electrode with a guarding ring on the other confining plate, with either homeotropic (for $\varepsilon_{\parallel}$) or low pre-tilt planar (for $\varepsilon_{\perp}$) surface alignment. For MLC2048, we found at frequency $f = 1$ kHz that $\varepsilon_{\parallel} = 11.47$, $\varepsilon_{\perp} = 8.51$, and $\Delta\varepsilon = \varepsilon_{\parallel} - \varepsilon_{\perp} = 2.96$, whilst at frequency $f = 30$ kHz we found that $\varepsilon_{\parallel} = 5.50$, $\varepsilon_{\perp} = 8.44$, and $\Delta\varepsilon = \varepsilon_{\parallel} - \varepsilon_{\perp} = -2.94$. Hence at 1 kHz MLC2048 is a nematic material that exhibits a positive dielectric anisotropy, $\Delta\varepsilon > 0$, and so, as with E7, an electric field at this frequency will exert a torque that acts to align the nematic n-director to be parallel to the local electric field direction. However, at 30 kHz MLC2048 exhibits a negative dielectric anisotropy, $\Delta\varepsilon < 0$, and so an electric field at this frequency will exert a torque that acts to align the nematic n-director to be orthogonal to the local electric field direction.

The surface tension, γ_{LV}, for the nematic materials, E7 and MLC2048 were measured using a pendant drop method. The density, ρ, of each material was measured from the contact angle, and hence volume, of a spherical cap-shaped sessile droplet of the material dispensed onto a Teflon AF treated glass substrate which was resting on a sensitive mass balance. We measured the values $\gamma_{LV} = (33.8 \pm 0.5) \times 10^{-3}$ N m^{-1} and $\rho_L = 1070 \pm 30$ kg m^{-3} for E7, and the values $\gamma_{LV} = (31.9 \pm 0.2) \times 10^{-3}$ N m^{-1} and $\rho_L = 1030 \pm 20$ kg m^{-3} for MLC2048.

To perform our voltage-forced wetting studies, a droplet of the nematic liquid crystal material was dispensed onto the centre of the electrode area of the device substrate using a Gilsen (0.1–2 μl) pipette. The electrical addressing of the interdigitated electrodes was performed using a TGA1244 arbitrary waveform generator (Thurlby Thander Instruments Ltd., Cambridge, UK) connected through a PZD700 amplifier (Trek Inc., Medine, New York, USA). A sinusoidal A.C. voltage with R.M.S. amplitude V_o, as shown in the schematic diagram in figure 1(b), was applied to alternate fingers of the interdigitated micro-stripe electrode array with the interposed electrode fingers held at earth potential. Figure 1(c) shows a y-z cross-section through the nematic liquid crystal droplet, electrodes, and substrate, within which figure 1(d) shows an expanded view of an 80 μm × 80 μm region within the droplet. When the voltage is applied this produces fringing electric fields that penetrate into the underside of the droplet, as depicted by the solid lines in figure 1(d). The nematic liquid crystal n-director orientation field, depicted by the open ellipses in figure 1(d) is distorted away from uniform vertical alignment by the action of these non-uniform electric fields coupling to

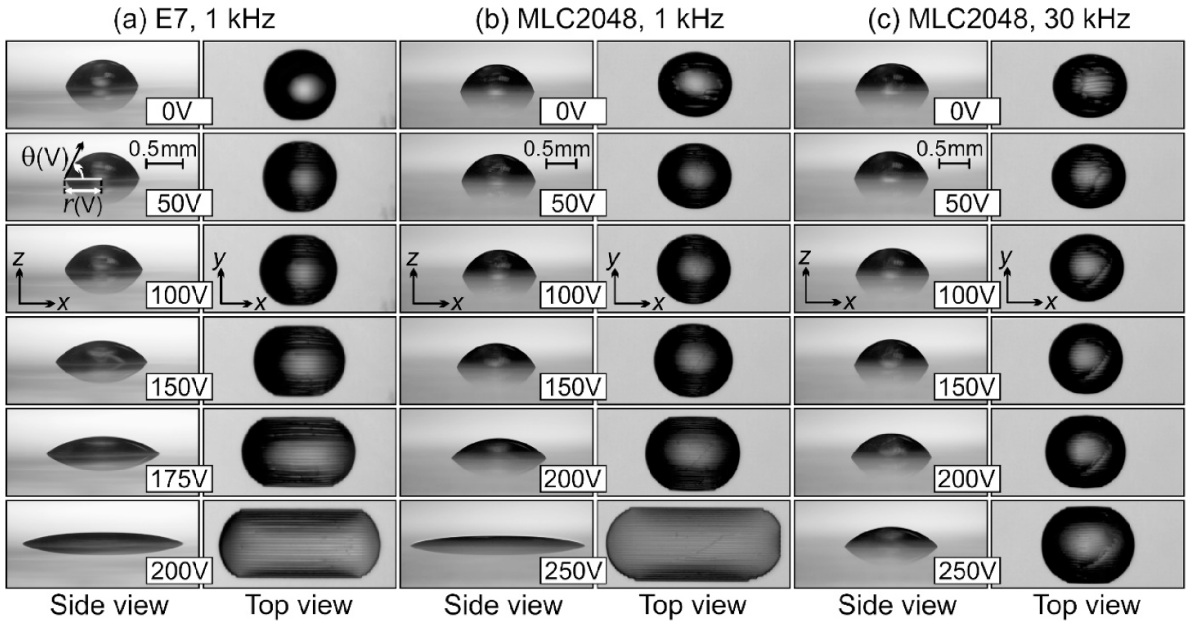

Figure 2. Microscope images of nematic liquid crystal droplets, resting on the device substrate, with the geometry as defined earlier in the schematic diagram in figure 1. The nematic material was E7 in panel (a), and MLC2048 in both the panels (b) and (c). Side and top views of each of the droplets are shown with different sinewave voltage R.M.S. amplitudes applied to the electrodes, with an A.C. frequency $f = 1$ kHz in both (a) and (b), and with $f = 30$ kHz in (c).

the uniaxial anisotropic polarisability of the adjacent nematic liquid crystal material.

3. Results

3.1. Voltage-forced spreading of nematic droplets

Figure 2 shows microscope images of the nematic liquid sessile crystal droplets used in our study. Snapshot pictures of the static droplets were taken simultaneously using two cameras, providing a side-view, from along the y-direction, and also a top view, from along the z-direction. Images of the droplets were captured using DCC1545M-GL cameras (Thorlabs) fitted with a 4× objective lens and lens tube. The top row of figure 2 shows pictures of the droplets with no voltage applied to the electrodes under the liquid when all of the electrodes in the stripe array were held at zero potential. The Teflon AF surface coating on the substrates provides a liquid repellent surface and a high equilibrium contact angle, θ_Y with no voltage applied, as defined in figure 1(a). The sessile droplet of E7, figure 2(a), had a substrate contact diameter, as defined in figure 1(a), of $2r_Y = 1.00 \pm 0.05$ mm (E7), a volume of 0.164 ± 0.006 μl, and an equilibrium contact angle of $\theta_Y = 71° \pm 1°$. The sessile droplet of MLC2048, shown in the top row both in figure 2(b) and in figure 2(c), had a contact diameter of $2r_Y = 1.24 \pm 0.05$ mm, a volume of 0.320 ± 0.004 μl, and an equilibrium contact angle of $\theta_Y = 72° \pm 1°$.

As well as providing a liquid repellent surface, the Teflon AF layer also imparted homeotropic (i.e. vertical) nematic surface alignment for both E7 and MLC2048, corresponding to the perpendicular alignment of the nematic n-director at the substrate [42]. This alignment was separately confirmed by polarising optical microscopy examination of the optical textures of E7 and MLC2048 between Teflon AF coated glass coverslips. The n-director alignment orientations at the E7-air and MLC2048-air surfaces were also found to be homeotropic, which was confirmed by separate polarising optical microscopy examination of thin free-standing layers of each of these nematic materials suspended in air, that were formed by stretching a film of the liquid across a hole in a piece of Mylar (polyethylene terephthalate) sheet.

The equilibrium contact angle θ_Y of an isotropic sessile liquid droplet is determined by three interfacial energies, γ_{LV} at the liquid-vapour interface (which is referred to as the surface tension), γ_{SV} at the solid-vapour interface, and $\gamma_{\rm SL}$ at the solid-liquid interface, according to Young's law, $\cos[\theta_Y] = (\gamma_{\rm SV} - \gamma_{\rm SL})/\gamma_{\rm LV}$ [43]. For general thermotropic calamitic nematic liquid crystal materials the anisotropy in the surface tension that is associated with different n-director alignment directions at the free surface, $\Delta\gamma_{\rm LV} = \gamma_{\rm LV\parallel} - \gamma_{\rm LV\perp}$, has been reported as being several orders of magnitude lower than $\gamma_{\rm LV}$ [44]. Furthermore, the elastic and surface anchoring forces are not significant in determining the equilibrium contact angle because they are many orders of magnitude lower than surface tension forces for a millimetre scale sessile nematic droplet. Our experiments were performed at a temperature of 22 ± 1 °C, which is deep into the nematic phase and well below the nematic-isotropic phase transition temperatures of E7 ($T_{\rm NI} = 58$ °C) and MLC2048 ($T_{\rm NI} = 105$ °C) where surface tension discontinuities would be observed. Hence Young's law will be applied here to the observed equilibrium contact angles of nematic materials [45, 46]. When first deposited, the nematic droplets adopted a spherical cap shape, as expected since the capillary length $L_{\rm c} = \sqrt{\gamma_{\rm LV}/[(\rho_L - \rho_{\rm air})\,g]}$,

where $g = 9.81$ ms^{-2}, was $L_c = 1.80 \pm 0.02$ mm for E7 and $L_c = 1.78 \pm 0.02$ mm for MLC2048. Since the size of our droplets were below L_c, no gravitational distortion was observed on the equilibrium droplet shape [47]. The contact angles θ_Y of the droplets did not vary as a function of azimuthal angle about their vertical axis in the z-direction and were found to be the same whether the droplet was viewed from along the x-direction or from along the y-direction to within the $\pm$ 1° accuracy of the measurement.

When we applied an A.C. voltage V_o of sufficiently high value to the electrode array underneath the sessile nematic droplets, this produced voltage-forced wetting, with spreading of the droplets predominantly parallel to the electrode micro-stripes in the x-direction. Panel (a) in figure 2 shows the effect of applying this spatially periodic potential to the underside of the sessile droplet of E7. Different voltage values of frequency 1 kHz were quasi-statically applied and the droplet was allowed sufficient time to reach equilibrium shape after each change in the value of the voltage. We define the voltage dependent contact angle $\theta(V_o)$, shown in figure 2(a), as the inner angle between the tangent to the droplet edge close to the contact line, and the horizontal substrate, viewed from the y-direction. The side view shows how the contact angle decreases and adopts a lower value that depends on the voltage, $\theta(V_o) < \theta_Y$, with a commensurate increase in the base width of the droplet in the x-direction. The width of the droplet in the y-direction does not change significantly as the voltage is applied. Hence the degree of wetting of the nematic liquid crystal E7 can be controlled by the magnitude of the voltage, from being a sessile droplet with a high contact angle, towards a spread film state at high voltages. As discussed in section 1, this phenomenon has previously been exploited for optical display and shutter devices based on voltage-forced wetting of dyed nematic liquid crystals [20–22]. We have further demonstrated, in figures 2(b) and (c), that a strongly frequency-dependent voltage-forced wetting effect occurs for the droplet of the highly dispersive nematic liquid crystal material MLC2048. Side and top view images of the shape of the droplet at different voltage values are shown in figure 2(b) for a 1 kHz waveform, and figure 2(c) for a 30 kHz waveform. Comparing the images for $V_o = 200$ V across the panels (a)–(c), it is clear that E7 spreads the most at this voltage value, accompanied by a significant increase in droplet contact width, MLC2048 at 1 kHz spreads to a lesser extent, and the lowest degree of spreading is exhibited by MLC2048 under the action of a 30 kHz voltage.

In figure 3 the voltage dependent contact angle values $\theta(V_o)$ for the nematic droplets that were depicted in figure 2 are plotted as a function of the applied A.C. voltage of amplitude V_o and frequency f. The data for the nematic liquid crystal material E7 ($f = 1$ kHz) are shown by the filled circles and the data for the material MLC2048 are shown by the open circles for $f = 1$ kHz and by the open diamonds $f = 30$ kHz. The E7 and the MLC2048 droplets have similar zero-voltage contact angle values, in the range 71°–73°. The overall shapes of the $\theta(V_o)$ versus V_o curves in figure 3(a) in all cases show a monotonic decrease (given an experimental scatter of ±1°)

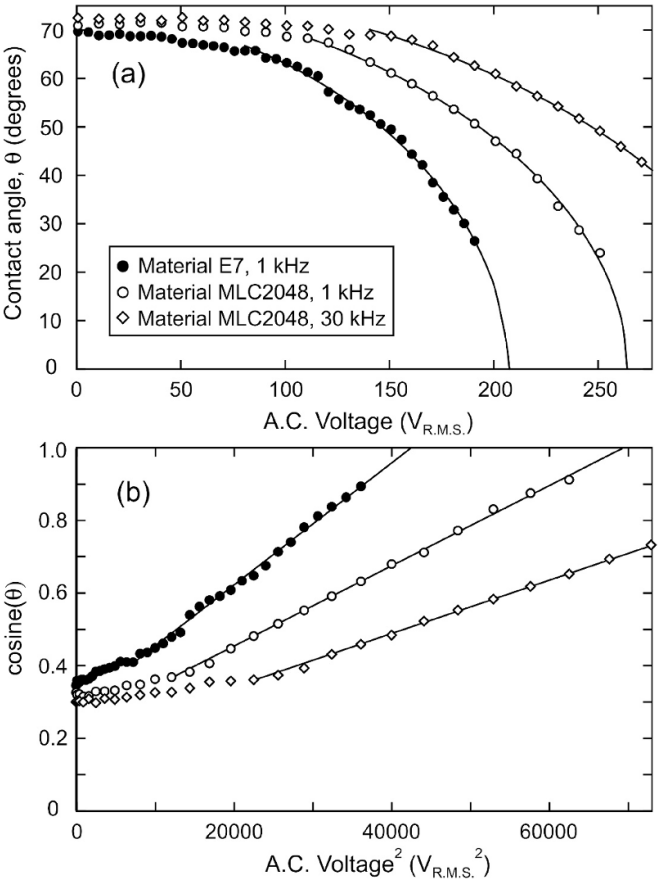

Figure 3. (a) Plot of the contact angle, $\theta(V_o)$, of the nematic liquid crystal droplets shown in figure 2 as a function of the R.M.S. value of the A.C. voltage, V_o, that was applied to the electrode array underneath each droplet. The filled circles show data for a sessile droplet of nematic material E7 subjected to a voltage of frequency 1 kHz, the open symbols show data for a sessile droplet of nematic material MLC2048 subjected to a voltage of frequency of either 1 kHz (open circles) or 30 kHz (open diamonds). In figure (b) the same data are re-plotted in a plot of the cosine of $\theta(V_o)$ versus the square of the voltage, V_o^2. In both figures, the solid lines show fits to equation (1) at the higher voltages.

in the contact angle as a function of the applied voltage, with very shallow negative slopes at low voltages, followed by the negative slopes of the curves becoming significantly steeper only at higher voltages. There are significant differences in the extent of the voltage-forced wetting for the different materials and frequencies studied. For example, for E7 a voltage of 165 V (1 kHz) reduces the contact angle to 44.4°, whilst for MLC2048 at 1 kHz a higher voltage of 210 V reduces the contact angle to 44.5°, and for MLC2048 at 30 kHz a still higher voltage of 270 V is needed to reduce the contact angle down to a similar level of 42.8°.

For an isotropic liquid with single isotropic dielectric permittivity ε_L and surface tension γ that spreads via voltage-forced dielectrowetting onto an interdigitated electrode array with micro-stripes (and gaps) of size w, the voltage dependent contact angle $\theta(V_o)$ is governed [17] by the equation,

$$\cos\left[\theta\left(V_o\right)\right] = \cos\left[\theta_Y\right] + \frac{\pi\varepsilon_o\left(\varepsilon_{\mathrm{L}} - 1\right)}{32\gamma w} V_o^2 = \cos\left[\theta_Y\right] + \beta V_o^2. \quad (1)$$

The second term in equation (1) is an electrostatic energy per unit contact area of the droplet divided by the droplet surface tension. The dielectrowetting coefficient β directly determines the magnitude of the voltage-forced spreading effect. The factor of $(\varepsilon_{\mathrm{L}} - 1)$ in β results from the droplet occupying an area on the surface that would otherwise be in the air, where the air has a dielectric constant close to unity. Equation (1) was derived by modelling the potential produced by the electrode array on the underside of the liquid droplet using a sinusoidal spatial dependence in the y-direction and an exponential decay into the droplet in the z-direction, $V(y,z) = \frac{1}{2}V_o\cos(\frac{1}{2}\pi y/w)e^{-\frac{1}{2}\pi z/w}$, whilst the thickness $h(y)$ of the liquid droplet fulfils the criterion $e^{-\pi h(y)/w} \ll 1$. The voltage dependent contact angle $\theta(V_o)$ predicted by equation (1) is independent of the volume of the liquid contained within the droplet, provided that the voltage forced spreading occurs with negligible change in the width of the droplet in the y-direction, which was shown to be the case for our system in figure 2. In reality, the spatial potential variation produced by co-planar interdigitated electrodes is a considerably more complex function of the geometric and material parameters of the system [48, 49], and the droplet shape evolves from being a spherical cap at zero voltage towards the idealised liquid stripe profile assumed in the derivation of equation (1) only at higher voltages. Even with the approximations described above, equation (1) has previously been found to be in good agreement with results for the voltage-forced dielectrowetting of a range of different volumes of isotropic dielectric liquids in air, and for the contact angle of different sized bubbles of air in isotropic dielectric liquids [17, 50].

We find here a regime of voltages where equation (1) can also provide an excellent description of the functional dependence of the contact angle for the voltage-forced dielectrowetting of anisotropic nematic liquid crystal materials. The data of figure 3(a) is replotted in figure 3(b) on a graph of the cosine of the contact angle $\theta(V_o)$ versus the square of the voltage, V_o^2. In both figures 3(a) and (b) there is a clear voltage delayed dielectrowetting effect, in which the agreement with equation (1) to each data set (solid lines) occurs only for voltages where $|\theta(V_o) - \theta_Y|$ exceeds 3°–4°, which is above $V_o > 85$ V for E7, above $V_o > 110$ V for MLC2048 at 1 kHz, and above $V_o > 140$ V for MLC2048 at 30 kHz. The values of the coefficients $\cos[\theta_Y]$ and β that were obtained from these higher voltage fits are given in table 1. We note that, even for isotropic liquids, at the lowest voltages there is often a region of flat or negligible gradient in the $\theta(V_o)$ versus V_o curves, which has been attributed to contact line pinning and hysteresis [17, 43].

We note that this measured value of the gradient β is highest for E7, which has a maximum possible permittivity of $\varepsilon_{\mathrm{Lmax}} = \varepsilon_{\parallel} = 18.96$, smaller for MLC2048 at 1 kHz, for which $\varepsilon_{\mathrm{Lmax}} = \varepsilon_{\parallel} = 11.47$, and lowest for MLC2048 at 30 kHz, for which $\varepsilon_{\mathrm{Lmax}} = \varepsilon_{\perp} = 8.44$. In the following section 3.2, we will now use Q-tensor modelling of nematic liquid crystal n-director distortion profiles to develop a more detailed understanding of how attendant electric field induced 2-dimensional n-director reorientation within a nematic droplet leads to the voltage delayed dielectrowetting effect, in which the high voltage linear $\theta(V_o)$ versus V_o^2 region develops only once the rate of change of n-director reorientation is becoming saturated.

Table 1. Values of the coefficients $\cos[\theta_Y]$ and β found from linear regression fitting of equation (1) to the data in figure 3(b), shown as the solid lines in the higher voltage regions.

Material, voltage frequency	Value of coefficient $\cos[\theta_Y]$	Value of coefficient β (V^{-2})
E7, 1 kHz	0.287 ± 0.005	$(1.68 \pm 0.02) \times 10^{-5}$
MLC2048, 1 kHz	0.233 ± 0.005	$(1.12 \pm 0.01) \times 10^{-5}$
MLC2048, 30 kHz	0.195 ± 0.006	$(0.74 \pm 0.01) \times 10^{-5}$

3.2. *Electric field induced nematic* n*-director reorientation within the droplet*

We examined the optical textures within the nematic liquid crystal droplets *in situ* as they were subject to different voltages. The optical microscope images shown in figure 4 were obtained using a 10× objective with the nematic droplet resting on the surface of the device substrate that was positioned on the microscope stage between crossed polarisers at ±45° to the x-direction. These snapshot microscope pictures were taken in transmission through the highest point of the droplet whilst different voltages were applied to the electrodes that were aligned horizontally on the substrate. The point of focus of the objective was adjusted to be close to the nematic-substrate boundary within the droplet. The white arrows indicate the positions of obvious abrupt localised changes in the nematic liquid crystal alignment direction. In figure 4(a) the top image shows the droplet of the nematic material E7 with 10 V (1 kHz) applied to the electrodes, for which horizontal zig-zag line defects are observed within the gaps between every adjacent micro-stripe electrode. In the top image of figure 4(b) similar horizontal line defects are also visible for MLC2048 subjected to a 10 V A.C. voltage with a frequency of 1 kHz, at which the material exhibits a positive dielectric anisotropy, the same sign as for E7. These line defects have a similar vertical width to the defects in E7 and are in a similar position between every adjacent electrode. In figure 4(c) the optical texture is shown in the top image for MLC2048 subjected to a 10 V A.C. voltage with a frequency of 30 kHz, at which the material exhibits a negative dielectric anisotropy. The horizontal zig-zag defects at this frequency are much less distinct, and there are also more prominent horizontal abrupt changes in the optical texture situated above every micro-stripe electrode (white arrows). These features were not as distinct for the cases where the dielectric anisotropy was positive in figures 4(a) and (b). In all cases in figure 4 the zig-zag defect lines are still clearly visible as the voltage is increased to 20 V and then to 40 V. At higher voltages of 60 V and above the defect lines become narrower and less distinct in all cases. The

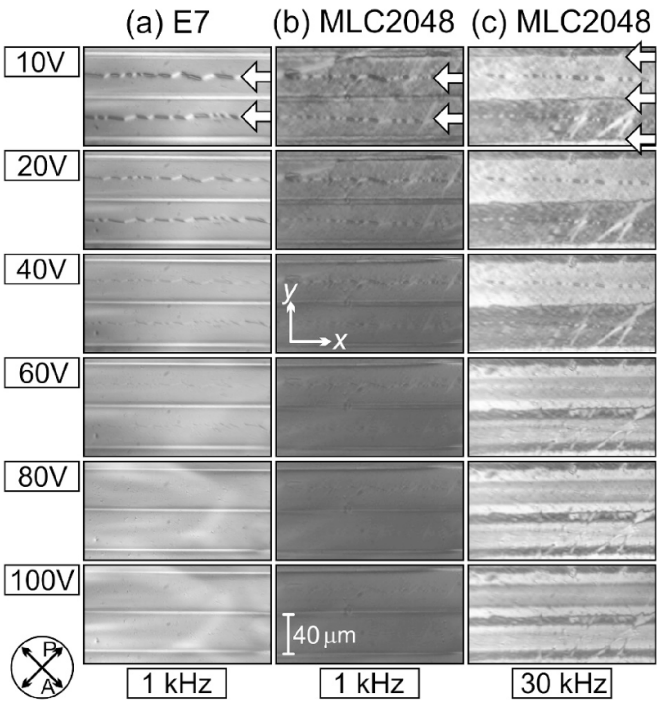

Figure 4. Polarising optical microscope images of nematic optical textures viewed in transmission between a crossed polariser (P) and an analyser (A). The nematic liquid crystal material was E7 in column (a), and MLC2048 in columns (b) and (c). The images were taken through sessile droplets, as shown in figure 2. Each row shows the optical textures resulting when a different sinewave voltage R.M.S. amplitude was applied to the electrodes on the substrate beneath the nematic material, with an A.C. frequency of $f = 1$ kHz in both (a) and (b), and of $f = 30$ kHz in (c). The white arrows indicate the positions of abrupt localised changes in the nematic liquid crystal alignment direction.

optical microscopy textures at 80 V and 100 V are very similar to one other, and we found a negligible change in their appearance for still further increases in the voltage.

The use of in-plane electric fields to switch a positive dielectric anisotropy nematic liquid crystal material has previously been proposed and studied, but in a fully confined geometry with solid upper and lower plates [25, 28, 29, 31]. Splay-bend defect walls were observed in these studies that were particularly distinct within the gaps between the micro-stripe electrodes on the lower solid plate. These splay-bend walls have also been referred to as Ising walls on account of the nature of the elastic distortions associated with these regions [51–53]. Zig-zag instabilities that arise in nematic Ising walls, similar to those observed in figure 4, have also been observed studied in a confined geometry with planar alignment on the upper and lower bounding plates [54, 55].

To provide insight into the nature of the optical textures shown in figure 4, we used mesoscopic Q-tensor theory [56] coupled to Maxwell's equations for the electric field, to calculate the spatial dependence of the nematic n-director orientation, $n(y,z)$, and the nematic order parameter in response to the electric fields $\mathbf{E}(y,z)$ produced by the micro-stripe electrodes in our device. Since this approach maintains the $n \equiv -n$ equivalence of the nematic n-director and also calculates a variable order parameter it allows the modelling of nematic defects in our structures. The calculations used commercial numerical partial differential equation solver software (COMSOL Multiphysics, COMSOL Ltd, Cambridge, UK) to minimise the total free energy of the system per unit area in the y-z plane. The free energy was formulated as an integral over a 2-dimensional region of the sum of thermotropic, distortion, and electrostatic energy densities together with the surface energy evaluated at the boundaries [56–60]. The spatially dependent electric field $\mathbf{E}(y,z)$ was obtained by solution of the Maxwell equation, $\nabla \cdot \mathbf{D} = 0$, where $\mathbf{D} = \varepsilon_o \varepsilon \mathbf{E}(y,z) = -\varepsilon_o \varepsilon \nabla V(y,z)$ and $\varepsilon(n(y,z))$ is the uniaxial nematic permittivity tensor and $V(y,z)$ is the spatially varying electric potential. The thermotropic coefficients of the Taylor expansion of the terms in the tensor order parameter $\mathbf{Q}$ [57] used in the model were, $a = 1.3 \times 10^4$ Nm^{-2}, $b = -1.6 \times 10^5$ Nm^{-2}, and $c = 3.9 \times 10^5$ Nm^{-2}. The equilibrium nematic order parameter was set at $S = 0.6$, and the surface anchoring energy was set at $W = 1.0 \times 10^3$ Nm^{-1}.

In figure 5 the double headed arrows show the spatially dependent static n-director field orientation angles $\theta(y,z)$ that we have calculated numerically using Q-tensor theory for E7 at 1 kHz (a), MLC2048 at 1 kHz (b), and for MLC2048 at 30 kHz (c) with the elastic constant values (K_1, K_2, and K_3) and permittivity values ($\varepsilon_{\parallel}$ and $\varepsilon_{\perp}$) given in section 2 of this report, and $K_{24} = 0$. We define $\theta = 0$ radians (equivalently $\theta = \pi$ radians, since $n \equiv -n$) for n-director orientation parallel to the horizontal y-axis, with $\theta = \pm\pi/2$ radians corresponding to the n-director orientated parallel to the vertical z-axis, with $\pi/2 < \theta < \pi$ describing the n-director tilted in the anti-clockwise sense relative to the vertical z-axis, and with $0 < \theta < \pi/2$ describing the n-director tilted in the clockwise sense relative to the vertical z-axis. The calculation domain was a 2-dimensional 80 μm $\times$ 80 μm y-z cross-section through a nematic layer subjected to the electric fields produced by coplanar micro-stripe electrodes (width $w = 20$ μm, shown by the filled rectangular boxes) running in the x-direction at the lower, nematic-solid, interface. The location of this domain in the droplet is adjacent to the substrate surface, as illustrated in figure 1(d). The free surface is significantly higher than the Q-tensor computational region. Since the thickness $h(y)$ of the liquid droplet fulfils the criterion $e^{-\pi h(y)/w} \ll 1$ (section 3.1), the electrostatic energy of the region above our computational domain is small and so the overall droplet volume does not affect our calculations. The domain width covered one period of the electric field variation, $4w$, and Neumann boundary conditions imposed a horizontal electric field direction between the electrodes at $z = 0$. The vertical domain height was chosen so that the numerical calculations converged within a practical timescale, whilst also providing sufficient decay of the potential variation $V(y,z)$, and the linked n-director distortion, in the z-direction. At the upper edge of the solution domain $\partial V/\partial z(y, z = 4w) = 0$, and periodic boundary conditions were implemented along the left- and right-hand edges of the domain, $n(y = 0, z) = n(y = 4w, z)$ and $V(y = 0, z) = V(y = 4w, z)$. The solid curved lines in figure 5 show the calculated equipotential contour lines $V(y,z)$ for a potential difference of either $V_o = 20$ V (equipotential lines shown for 1 V

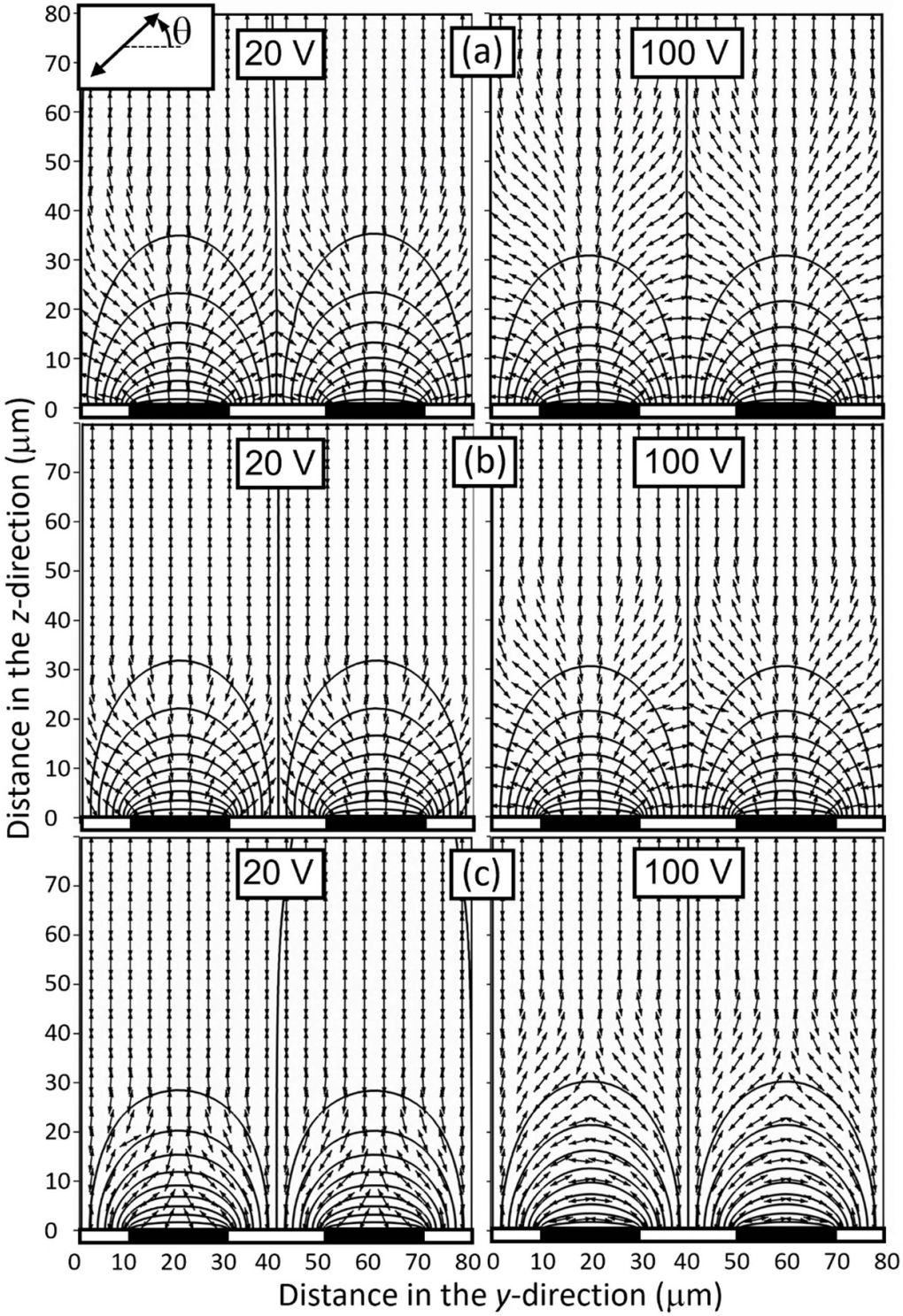

Figure 5. The two-dimensional spatial variation in the nematic n-director orientation $\theta(y,z)$, shown by double headed arrows, that was calculated using nematic Q-tensor theory. The simulation domains represent a y-z cross-section through a nematic layer subjected to the electric fields produced by orthogonal co-planar micro-stripe electrodes at the positions of the filled rectangles on the lower interface. The solid curved lines show equipotential contours when the potential difference between the electrodes was either 20 V (1 V increments, left column) or 100 V (5 V increments, right column). The Q-tensor calculations were performed using the elastic and dielectric parameters given in section 2 for E7 at 1 kHz A.C. voltage frequency (a), for MLC2048 at 1 kHz (b), and for MLC2048 at 30 kHz (c).

increments, left column) or $V_o = 100$ V (5 V increments, right column).

In the absence of any applied voltage, the homeotropic alignment at the upper and lower interfaces oriented the entire n-director field $n(y,z)$ vertically at $\theta(y,z) = \pi/2$ radians. The degree of voltage-induced local reorientation away from $\theta = \pi/2$ is determined by the local magnitude and direction of the spatially dependent electric field $\mathbf{E}(y,z)$, by the magnitude and

sign of the dielectric anisotropy $\Delta\varepsilon = \varepsilon_{\parallel} - \varepsilon_{\perp}$, and by elastic coupling to the surface anchoring. For a positive dielectric anisotropy nematic material with $\Delta\varepsilon > 0$, which applies to E7 in figure 5(a) and to MLC2048 at 1 kHz in figure 5(b), the greatest degree of *n*-director reorientation occurs in the vicinity of the inter-electrode gaps. This occurs because when $\Delta\varepsilon > 0$ the electrostatic forces act to align the *n*-director parallel to the substantially horizontal local electric field direction in the gaps, i.e. orthogonally to the equipotential contour lines. The *n*-director tilt orientation directions are in opposite senses in the vicinity of neighbouring electrodes in figures 5(a) and (b), with $\theta < \pi/2$ adjacent to the electrode edge at $(y, z) = (30, 0)$ μm, and with $\theta > \pi/2$ adjacent to the electrode edge at $(y, z) = (50, 0)$ μm. This consequence of the opposing directions of the fringing electric fields at neighbouring electrode edges creates alternating regions of opposing tilt direction which are separated by splay-bend elastic distortion walls [51–53]. The Q-tensor calculations of the spatial variation in the nematic order also revealed that the significant electrostatic constriction of the nematic distortion within the gap creates line disclinations, with attendant localised reduction in the order parameter, within the splay-bend walls within the electrode gap regions.

For a negative dielectric anisotropy nematic material with $\Delta\varepsilon < 0$, which applies to MLC2048 at 30 kHz in figure 5(c), electrostatic forces act to align the *n*-director orthogonal to the local electric field direction, and hence parallel to the equipotential contour lines. The *n*-director reorientation now occurs predominantly above the electrodes micro-stripes where the electric field is substantially vertical. Here the opposing directions of the fringing electric fields towards each side of an individual electrode result in an *n*-director reorientation tilt with $\theta < \pi/2$ on the left-hand side of an electrode, and $\theta > \pi/2$ on the right-hand side of the same electrode. The electrostatic constriction of the nematic distortion when $\Delta\varepsilon < 0$ is now above the centre of the electrode. This leads to the creation of distinct splay-bend walls positioned above the electrode micro-stripes, as shown in figure 5(c), instead of being within the gap when $\Delta\varepsilon > 0$, as shown in figures 5(a) and (b) [30].

The predictions of our mesoscopic Q-tensor theory simulations, shown in figure 5, are in accord with the key experimental observations on the optical textures shown in figure 4. The splay-bend walls are located within the middle of the inter-electrode gap when $\Delta\varepsilon > 0$, which is the case for E7 in figure 4(a) (experiment) and figure 5(a) (simulation) and for MLC2048 at 1 kHz in figure 4(b) (experiment) and figure 5(b) (simulation). However, the most prominent region of reorientation is located above the centre of the micro-stripe electrodes when $\Delta\varepsilon < 0$, which is the case for MLC2048 at 30 kHz in figure 4(c) (experiment) and figure 5(c) (simulation). For both the $\Delta\varepsilon < 0$ and the $\Delta\varepsilon > 0$ cases the electrostatic constriction effect shown in figure 5 is stronger at 100 V potential difference compared to at 20 V, which is consistent with the experimental observations in figure 4 that the distortion surrounding the defect line becomes narrower and so less optically distinct as the voltage is increased.

We used our numerical Q-tensor simulations to calculate the total free energy of the 2-dimensional domain in the *y*-*z* plane shown in figure 5 as an integral of a sum of thermotropic, distortion, and electrostatic energy density components, at a range of applied voltages. Figure 6 shows a plot of the electrostatic component of the total free energy divided by the square of the applied voltage, W_e/V^2, versus the R.M.S. voltage, V, for E7 at 1 kHz A.C. voltage frequency (filled circle symbols), for MLC2048 at 1 kHz (open circles), and for MLC2048 at 30 kHz (open diamond). In each case the value of W_e/V^2 increases the most steeply at low voltages followed by a saturation effect where W_e/V^2 exhibits a much shallower increase as a function of voltage between $V = 50$ V and $V = 200$ V. The steeper increase of W_e/V^2 at lower voltages reflects the initial development of significant elastic distortion within the nematic *n*-director field accompanied by the formation of splay-bend walls. A high electric field acting within a nematic liquid crystal material will exert a torque on the nematic *n*-director which acts to align the largest component of the dielectric permittivity with the local direction of the field. At higher voltages, where significant alignment has already occurred, there is a lower rate of change with voltage in the distortion of the *n*-director field. This is consistent with our experimental observations in figure 4 that the optical textures for 80 V and 100 V are very similar in appearance.

A single voltage dependent capacitance of the nematic layer on an interdigitated electrode system can be expressed as an effective permittivity value $\varepsilon_{\text{eff}}(V)$ by taking into account the specific electrode geometry. This is the relevant permittivity value that determines the magnitude of voltage-forced wetting by setting $\varepsilon_{\text{L}} = \varepsilon_{\text{eff}}$ in the dielectrowetting equation (1). Our Q-tensor calculation results plotted in figure 6 permit the direct prediction of the value of $\varepsilon_{\text{eff}}(V)$, and hence also the value of

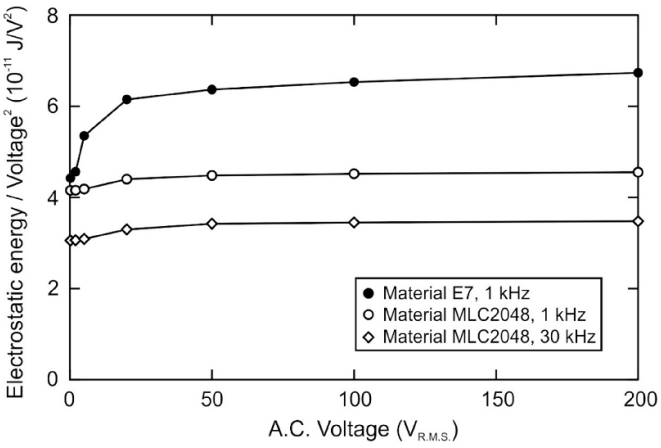

Figure 6. Electrostatic energy of a homeotropic nematic layer subjected to electric fields produced by co-planar micro-stripe electrodes. The electrostatic energy was obtained from numerical Q-tensor theory calculations using the elastic and dielectric parameters given in section 2. Figure 5 previously showed the calculated 2-dimensional spatial variation in the nematic *n*-director orientation, $\theta(y, z)$, and the electric potential $V(y, z)$ for the cases of $V = 20$ V and $V = 100$ V. Here, the energy divided by the square of the applied voltage, W_e/V^2, is plotted against the R.M.S. voltage, V, for E7 at 1 kHz A.C. voltage frequency (filled circle symbols), for MLC2048 at 1 kHz (open circles), and for MLC2048 at 30 kHz (open diamonds).

the dielectrowetting coefficient β. In this analysis it is assumed that the calculated spatially dependent static n-director fields shown in figure 5 do not vary in the x-direction, and that the energy values given in figure 6 scale in proportion to the width in the y-direction, which is a reasonable approximation provided that the (voltage independent) contact diameter $2r_Y$ in the y-direction is significantly larger than one period of the electrode pattern $2w$, i.e. $r_Y \gg w$, which holds for our system. Our specific electrode geometry is firstly accounted for by setting $\Delta\varepsilon = 0$ in the Q-tensor model which gave $\varepsilon_{\text{eff}} = 4.269 \times 10^{-12}\left(W_e/V^2\right)$. Using this relationship with the Q-tensor simulation results for the electrostatic energy plotted in figure 6 for 200 V, gives $\varepsilon_{\text{eff}} = 15.78$ for E7 (1 kHz), $\varepsilon_{\text{eff}} = 10.67$ for MLC2048 (1 kHz), and $\varepsilon_{\text{eff}} = 8.14$ for MLC2048 (30 kHz). For MLC2048 in particular, these effective permittivity values have saturated close to the larger out of the material's two uniaxial permittivity values at the relevant frequency, at 1 kHz we find $\varepsilon_{\text{eff}} = 10.67$ when $\varepsilon_{\text{Lmax}} = \varepsilon_{\parallel} = 11.47$, and at 30 kHz we find $\varepsilon_{\text{eff}} = 8.14$ when $\varepsilon_{\text{Lmax}} = \varepsilon_{\perp} = 8.44$.

In our system $w = 20$ μm, and so the dielectrowetting coefficient predicted by equation (1) is given by $\beta = 4.34 \times 10^{-8}\ (\varepsilon_{\text{eff}} - 1)/\gamma$. Substituting in the relevant surface tension values γ and the effective permittivity values obtained from the Q-tensor simulation this predicts that $\beta = 1.90 \times 10^{-5}$ V^{-2} for E7 (1 kHz), $\beta = 1.32 \times 10^{-5}$ V^{-2} for MLC2048 (1 kHz), and $\beta = 0.97 \times 10^{-5}$ V^{-2} for MLC2048 (30 kHz). Whilst these values are between 13% (E7) and 31% (MLC2048, 30 kHz) higher than the experimental values found, table 1, the level of agreement between the theory and experiment is remarkable given the significant approximations that have been made to derive the analytical dielectrowetting expression in equation (1) and given that no free fitting parameters have been used in the Q-tensor simulations. In the following section 3.3, we will now demonstrate and elucidate the frequency control of the value of the dielectrowetting coefficient β in the highly dispersive nematic liquid crystal material MLC2048.

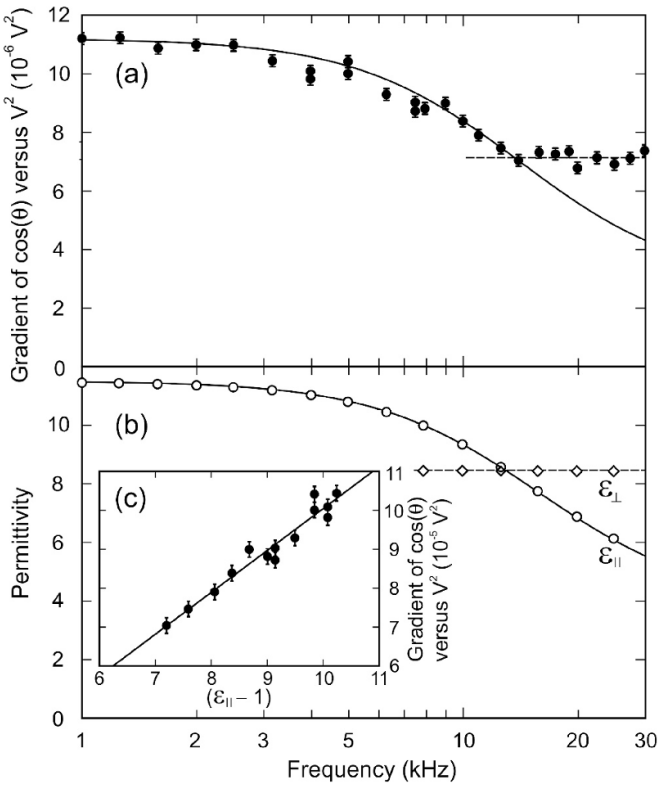

Figure 7. (a) Plot of the fitted value of β as a function of frequency for dielectrowetting of a sessile droplet of MLC2048. (b) Plot of the measured dielectric permittivity values for MLC2048 at 23 ± 1 °C as a function of frequency, with parallel permittivity values $\varepsilon_{\parallel}$ shown by the open circles and perpendicular permittivity values $\varepsilon_{\perp}$ shown by the open diamonds. In (a) and (b) separate frequency-dependent Debye relaxation fits to the data are shown by solid lines, and averages of data over a range of frequency values are shown by dashed lines. The inset figure in (b) plots the gradient data from (a) against the value of $(\varepsilon_{\parallel} - 1)$ from the Debye fit to the data for $\varepsilon_{\parallel}$ in (b).

3.3. *Frequency-dependent voltage-forced spreading of a highly dispersive nematic material*

Figure 7(a) shows the results from our further detailed study of the voltage-forced wetting of a sessile droplet of MLC2048 as a function of the frequency of the driving voltage, now covering the range between 1 kHz and 30 kHz. In this frequency interval there is a pronounced Debye frequency relaxation of the value of the material's permittivity $\varepsilon_{\parallel}$ parallel to the nematic n-director [36, 37]. In figure 7(a) the value of the dielectrowetting coefficient β is plotted for a number of discrete frequencies in the range 1 kHz to 30 kHz. For each frequency, the value of β was obtained from a linear regression fit to the higher voltage data on a $\cos[\theta(V_o)]$ versus V_o^2 plot, following the same procedure as previously shown in figure 3(b) for 1 kHz and for 30 kHz. For intermediate frequencies, especially close to 14 kHz, a reduced set of voltage values were applied for short time intervals in order to minimise dielectric heating of the material during the measurements. We find that our experimental values of β, plotted in figure 7(a), exhibit a decrease as a function of frequency f at the lower frequencies investigated, with the steepest negative gradient between 8 kHz and 14 kHz, and then the value of β remains constant (to within experimental scatter) at the higher frequencies between 14 kHz and 30 kHz. Hence, for frequency values up to 14 kHz, we demonstrate frequency control of the degree of voltage-forced wetting in the highly dispersive nematic liquid crystal material MLC2048.

Figure 7(b) plots the values of the uniaxial dielectric permittivities, $\varepsilon_{\parallel}$ (open circle symbols) and $\varepsilon_{\perp}$ (open diamond symbols), for the nematic liquid crystal MLC2048 that we measured using the procedure described in section 2. A significant contribution to the $\varepsilon_{\parallel}$ and $\varepsilon_{\perp}$ permittivity values of calamitic nematic liquid crystal materials arises from the bulk dielectric polarisation induced by partial reorientation of permanent molecular dipoles to align with an applied field [57, 61]. For the highly dispersive nematic material MLC2048 a low frequency relaxation of the magnitude of $\varepsilon_{\parallel}$ results from hindered rotation about the short molecular axes [36, 37, 62]. In Debye theory [63, 64] it is assumed that the magnitude of the induced dielectric polarisation evolves exponentially

with time, which leads to a well defined relaxation frequency f_R, below which the reorientation mechanism contributes to the dielectric susceptibility, but above which it does not contribute. An exponential time dependence of the component of the polarisation parallel to the n-director has previously been used successfully to describe the re-orientation dynamics of MLC2048 [40, 62]. The solid line in figure 7(b) shows the excellent fit to the data for $\varepsilon_{||}$ for the batch of the material MLC2048 used in our study by the Debye relaxation function, $\varepsilon_{||D}(f) = \varepsilon_{||o} + \left[\left(\varepsilon_{||o} - \varepsilon_{||\infty}\right) / \left(1 + (f/f_R)^2\right)\right]$ [64], with $\varepsilon_{||o} = 11.53 \pm 0.05$, $\varepsilon_{||\infty} = 3.90 \pm 0.05$, and $f_R = 15.9 \pm 0.5$ kHz. The permittivity perpendicular to the nematic *n*-director, $\varepsilon_\perp$, does not vary significantly with frequency in the range 1 kHz to 30 kHz for MLC2048. The average value over this range, $\varepsilon_\perp = 8.46 \pm 0.05$, is shown by the horizontal dashed line in figure 7(b).

We find an excellent agreement between the shape of the plot of the dielectrowetting coefficient β for MLC2048 versus frequency f, figure 7(a), and the highest value out of the two frequency-dependent uniaxial permittivity values $\varepsilon_{||}$ and $\varepsilon_\perp$ for MLC2048, figure 7(b). This observation is entirely consistent with the results from our Q-tensor modelling, described above in section 3.2, that showed how a permittivity that is close to the highest permittivity in the system at a particular frequency is the appropriate factor ε_L in the coefficient β in equation (1) for MLC2048. To explore this outcome more quantitatively, firstly we compare the $\beta(f)$ data in figure 7(a) with a Debye relaxation function. In figure 7(a) the solid line shows a fit of the data at the lower frequencies to the function $\beta_D(f) = \beta_o + \left[(\beta_o - \beta_\infty) / \left(1 + (f/f_o)^2\right)\right]$, with $\beta_o = (1.12 \pm 0.01) \times 10^{-5}$ V^{-2}, $\beta_\infty = (0.28 \pm 0.01) \times 10^{-5}$ V^{-2}, and $f_o = 14.1 \pm 0.6$ kHz. The Debye relaxation function provides a good description of the frequency dependence of β up to 14 kHz, which is somewhat below the relaxation frequency f_R found for the $\varepsilon_{||}$ data. Above 14 kHz the average value of β in the frequency independent region is shown by the dotted horizontal line at $\beta_{ave} = (0.71 \pm 0.08) \times 10^{-5}$ V^{-2}. Secondly, in the inset figure in 7(b) we plot the experimental value of β at a given frequency against $\left(\varepsilon_{||} - 1\right)$ where $\varepsilon_{||} = \varepsilon_{||D}(f)$. We plot $\left(\varepsilon_{||} - 1\right)$, rather than $\varepsilon_{||}$, since the former is the term in which the permittivity appears in equation (1). The plot covers frequencies in the range 3 kHz to 14 kHz, over which there is a sufficient variation of the values of both β and $\varepsilon_{||}$ with frequency to explore. We find clear linear relationship between these two quantities, with the solid line showing the linear regression fit $\beta = (1.08 \pm 0.07)\left(\varepsilon_{||} - 1\right) - (0.73 \pm 0.68)$ V^{-2}, with the low intercept value meaning that this is close to a direct proportionality.

4. Conclusions

We have demonstrated voltage-forced wetting and spreading of sessile droplets of two different nematic liquid crystal materials, the well characterised mixture E7, and the highly dispersive mixture MLC2048 and, for MLC2048, frequency-dependent controllable spreading. These materials have anisotropic physical properties, including significant differences between their dielectric permittivity values parallel to and perpendicular to the nematic *n*-director, $\varepsilon_{||}$ and $\varepsilon_\perp$ respectively. The induced wetting was achieved by the action of dielectrophoresis forces that polarise the region of the liquid adjacent to an interdigitated electrode array, on the solid surface, that is subjected to an A.C. voltage of R.M.S value V_o. At higher voltages the voltage induced reduction in contact angle $\theta(V_o)$ was found to obey the linear relationship, $\cos[\theta(V_o)] = \cos[\theta_Y] - \beta V_o^2$, where β is the dielectrowetting coefficient, as found previously in the literature but for isotropic liquid droplets in air [17]. Our Q-tensor calculations have elucidated the nature of the nematic optical textures of the droplet under voltage that we observed using polarising optical microscopy. By comparison between the experimental textures and the Q-tensor simulations we have explained how this voltage-delayed linear regime occurs once the rate of change with voltage of the overall distortion to the *n*-director field has substantially saturated.

The nematic liquid crystal material MLC2048 has a pronounced Debye frequency relaxation of the value of the material's permittivity $\varepsilon_{||}$ parallel to the nematic *n*-director. This provides frequency control of the permittivity which permits study of how the permittivity value governs the degree of dielectrowetting whilst the other properties of the liquid, including its surface tension, are kept constant. We found that the degree of voltage-forced wetting of MLC2048 at a particular frequency is determined by which of the material's two uniaxial permittivity values, $\varepsilon_{||}$ and $\varepsilon_\perp$, is largest at that frequency. For frequencies up to 14 kHz where $\varepsilon_{||} > \varepsilon_\perp$, we found that the frequency dependence of the dielectrowetting coefficient β is directly proportional to the value $\left(\varepsilon_{||} - 1\right)$ to a very good approximation. Our results offer the possibility of frequency control, in addition to voltage control, of the operation of optofluidic devices such as reconfigurable lenses and voltage programmable optical shutters or coloured filters [16, 20–23].

Data availability statement

The data presented in this study are available on request from the corresponding author.

Acknowledgments

We gratefully acknowledge useful discussions with G McHale at Edinburgh University and J Walton at the University of Glasgow, and R P Tuffin and O Parri at Merck Chemicals Ltd for providing nematic liquid crystal materials.

Author contributions

Conceptualization, C V B, A S B, A M J E, N J M, I C S, A S; Methodology, C V B, A S B, A M J E, N J M, I C S, A S; Software, N J M; Formal analysis, C V B, A S B, A M J E,

N J M, A S; Investigation, C V B, A S B, A M J E, N J M, I C S, A S;

Resources, C V B, A S B, A M J E, N J M, A S; Data curation, C V B, A S B, A M J E, A S; Writing—original draft preparation, C V B.; Writing—review and editing, C V B, A S B, N J M, I C S; Supervision, C V B, N J M; Project administration, C V B, N J M; Funding acquisition, C V B, N J M; All authors have read and agreed to the published version of the manuscript.

Conflict of interest

The authors declare no conflict of interest.

Ethics statement

No ethical approval required.

Funding

A Saxena and A S Bhadwal were funded by Merck Chemicals Ltd and by Nottingham Trent University PhD Scholarships. C V Brown, A M J Edwards and N J Mottram were funded by the UK EPSRC (Grant Nos. EP/J009865/1, EP/R042276/1, and EP/J009873/1, respectively).

ORCID iDs

Carl V Brown https://orcid.org/0000-0002-1559-3238
Akhshay S Bhadwal https://orcid.org/0000-0002-6700-2604
Andrew M J Edwards https://orcid.org/0000-0003-3338-1287
Antariksh Saxena https://orcid.org/0000-0002-5390-6629
Nigel J Mottram https://orcid.org/0000-0002-7265-0059

References

[1] Pohl H A 1978 Dielectrophoresis: the behavior of neutral matter in nonuniform electric fields *Cambridge Monographs on Physics* (London: Cambridge University Press) p 1
[2] Hughes M P 2016 Fifty years of dielectrophoretic cell separation technology *Biomicrofluidics* **10** 032801
[3] Maidin N N M, Buyong M R, Rahim R A and Mohamed M A 2021 Review: dielectrophoresis applications in biomedical field and future perspectives in biomedical technology *Electrophoresis* **42** 2033–59
[4] Waheed W, Omar Z, Sharaf A A and Eiyad A-N 2021 Dielectrophoresis-field flow fractionation for separation of particles: a critical review *J. Chromatogr.* A **1637** 461799
[5] Pesch G R and Du F 2021 A review of dielectrophoretic separation and classification of non-biological particles *Electrophoresis* **42** 134–52
[6] Pellat H 1895 Mesure de la force agissant sur les diélectriques liquides non électrisés placés dans un champ élitrique *C. R. Acad. Sci.* **119** 691–4
[7] Jones T B, Gunji M, Washizu M and Feldman M J 2001 Dielectrophoretic liquid actuation and nanodroplet formation *J. Appl. Phys.* **89** 1441–8
[8] Wexler A D, López Sáenz M, Schreer O, Woisetschläger J and Fuchs E C 2014 The preparation of electrohydrodynamic bridges from polar dielectric liquids *J. Vis. Exp.* **91** e51819
[9] Jones T B, Wang K-L and Yao D-J 2004 Frequency-dependent electromechanics of aqueous liquids: electrowetting and dielectrophoresis *Langmuir* **20** 2813–8
[10] Su X, Ren H and Wu S-T 2013 Dielectrophoretically tunable optofluidic devices *J. Phys. D: Appl. Phys.* **46** 483001
[11] Cheng Y, Cao J and Hao Q 2021 Optical beam steering using liquid-based devices *Opt. Lasers Eng.* **146** 106700
[12] Edwards A M J, Brown C V, Newton M I and McHale G 2018 Dielectrowetting: the past, present and future *Curr. Opin. Colloid Interface Sci.* **36** 28–36
[13] Barman J 2019 Wettability manipulation by interface-localized liquid dielectrophoresis: fundamentals and applications *Micromachines* **10** 329
[14] Geng H, Feng J, Stabryla L M and Cho S K 2017 Dielectrowetting manipulation for digital microfluidics: creating, transporting, splitting, and merging of droplets *Lab Chip* **17** 1060–8
[15] Brown C V, Wells G G, Newton M I and McHale G 2009 Voltage-programmable liquid optical interface *Nat. Photon.* **3** 403–5
[16] Cheng C-C, Alex Chang C and Andrew Yeh J 2006 Variable focus dielectric liquid droplet lens *Opt. Express* **14** 4101–6
[17] McHale G, Brown C V, Newton M I, Wells G G and Sampara N 2011 Dielectrowetting driven spreading of droplets *Phys. Rev. Lett.* **107** 186101–4
[18] Brown C V, McHale G and Trabi C L 2015 Dielectrophoresis-driven spreading of immersed liquid droplets *Langmuir* **31** 1011–6
[19] Funada F, Schadt M, Toriyama K, Takatsu H, Gotoh Y and Sekiya T 2014 Liquid crystal materials *The Liquid Crystal Display Story* ed N Koide (Tokyo: Springer) p 3
[20] Ren H, Xu S and Wu S-T 2011 Voltage-expandable liquid crystal surface *Lab Chip* **11** 3426–30
[21] Ren H and Shin-Tson W 2011 Fringing field stretching of a pillared liquid crystal droplet *J. Phys. D: Appl. Phys.* **44** 375301–5
[22] Russell A C, Hsieh W L, Chen K C and Heikenfeld J 2015 Experimental and numerical insights into isotropic spreading and deterministic dewetting of dielectrowetted films *Langmuir* **31** 637–42
[23] Wang X, Zhang G and Ren H 2016 Large-area optical switch using surface-expandable liquid droplets *J. Disp. Technol.* **12** 1565–9
[24] Lueder E 2011 Liquid crystal displays addressing schemes and electro-optical effects *Wiley-SID Series in Display Technology* 2nd edn (New York: Wiley)
[25] Soref R A 1974 Field effects in nematic liquid crystals obtained with interdigital electrodes *J. Appl. Phys.* **45** 5466–8
[26] Kiefer R, Weber B, Windscheid F and Baur G 1992 *Proc. 12th Int. Display Research Conf. "Japan Display'92," Int. Conf. Center Hiroshima* (*Hiroshima, Japan, 12–14 October 1992*) (Society for Information Display, the Institute of Television Engineers of Japan) p 547
[27] Masahito O and Kondo K 1995 Electro-optical characteristics and switching behavior of the in-plane switching mode *Appl. Phys. Lett.* **67** 3895
[28] Lee S H, Kim H Y, Park I C, Rho B G, Park J S, Park H S and Lee C H 1997 Rubbing-free, vertically aligned nematic liquid crystal display controlled by in-plane field *Appl. Phys. Lett.* **71** 2851–3
[29] Kim K-H, Park S-B, Shim J-U, Souk J-H and Chen J 1998 New LCD modes for wide-viewing-angle applications *SID Int. Symp. Dig. Tech. Pap. 29* pp 1085–8

[30] Hsieh C T, Huang C Y and Lin C H 2007 In-plane switching dual-frequency liquid crystal cell *Opt. Express* **15** 11685–90
[31] Choi T-H, Woo J-H, Choi Y and Yoon T-H 2016 Effect of two-dimensional confinement on switching of vertically aligned liquid crystals by an in-plane electric field *Opt. Express* **24** 20993–1000
[32] Gray G W, Harrison K J and Nash J A 1973 New family of nematic liquid crystals for displays *Electron. Lett.* **9** 130–13122
[33] Ashford A, Constant J, Kirton J and Raynes E P 1973 Electro-optic performance of a new room-temperature nematic liquid crystal *Electron. Lett.* **9** 118–20
[34] Oswald P and Pieranski P 2005 *Nematic and Cholesteric Liquid Crystals* (Boca Raton, FL: Taylor & Francis)
[35] Khoo I C 2007 *Liquid Crystals* 2nd edn (New York: Wiley)
[36] Schadt M 1981 Dielectric heating and relaxations in nematic liquid crystals *Mol. Cryst. Liq. Cryst.* **66** 319–36
[37] Schadt M 1982 Low-frequency dielectric relaxations in nematics and dual-frequency addressing of field effects *Mol. Cryst. Liq. Cryst.* **89** 77–92
[38] Pishnyak O, Sato S and Lavrentovich O D 2006 Electrically tunable lens based on a dual-frequency nematic liquid crystal *Appl. Opt.* **45** 4576–82
[39] Xianyu H, Wu S-T and Lin C-L 2009 Dual frequency liquid crystals: a review *Liq. Cryst.* **36** 717–26
[40] Mottran N J and Brown C V 2006 Pulsed addressing of a dual-frequency nematic liquid crystal *Phys. Rev.* E **74** 1
[41] Xiong J, Chen R and Wu S-T 2019 Device simulation of liquid crystal polarization gratings *Opt. Express* **27** 18102–12
[42] Bhadwal A S, Mottram N J, Saxena A, Sage I C and Brown C V 2020 Electrically controlled topological micro cargo transportation *Soft Matter* **16** 2961–297
[43] De Gennes P G 1985 Wetting: statics and dynamics *Rev. Mod. Phys.* **57** 827–63
[44] Korjenevsky V A and Tomilin M G 1993 Experimental investigation of the surface energy of a nematic liquid crystal *Liq. Cryst.* **15** 643–9
[45] Rey A D 2000 The Neumann and Young equations for nematic contact lines *Liq. Cryst.* **27** 195–200
[46] Zaki Ewiss M A, Nabil G, Schlagowski S and Herminghaus S 2004 Wetting behaviour of 5CB and 8CB and their binary mixtures above the isotropic transition *Liq. Cryst.* **31** 557–66
[47] De Gennes P G, Brochard-Wyart F and Quéré D 2004 *Capillarity and Wetting Phenomena Drops, Bubbles, Pearls, Waves* (New York: Springer) (https://doi.org/10.1007/978-0-387-21656-0)
[48] Morgan H, Izquierdo A G, Bakewell D, Green N G and Ramos A 2001 Green's function-based control-oriented modeling of electric field for dielectrophoresis *J. Appl. Phys.* **34** 1553
[49] Den Otter M W 2002 Approximate expressions for the capacitance and electrostatic potential of interdigitated electrodes *Sens. Actuators* A **96** 140
[50] Roberts A, Newton M I, Sage I C, Ledesma-Aguilar R, McHale G, Brown C V and Edwards A M J 2021 Bubble control, levitation, and manipulation using dielectrophoresis *Adv. Mater. Interfaces* **8** 2001204
[51] Brochard F 1972 Mouvements de parois dans une lame mince nématique *J. Phys.* **33** 607–11
[52] Cladis P E and Torza S 1975 Growth of a smectic A from a bent nematic phase and the smectic light valve *J. Appl. Phys.* **46** 584
[53] Chevallard C and Clerc M G 2001 Inhomogeneous Fréedericksz transition in nematic liquid crystals *Phys. Rev.* E **65** 011708
[54] Chevallard C, Clerca M, Coullet P and Gilli J-M 2000 Interface dynamics in liquid crystals *Eur. Phys. J.* E **1** 179–88
[55] Andrade-Silva I, Clerc M G and Odent V 2014 Zig-zag wall lattice in a nematic liquid crystal with an in-plane switching configuration *Phys. Rev.* E **90** 022504
[56] Priestly E B, Wojtowicz P J and Sheng P 1976 *Introduction to Liquid Crystals* (New York: Plenum)
[57] De Gennes P G and Prost J 1993 *The Physics of Liquid Crystals* (New York: Oxford University Press)
[58] Schophol N and Sluckin T J 1987 Defect core structure in nematic liquid crystals *Phys. Rev. Lett.* **59** 2582
[59] Virga E G 1994 *Variational Theories for Liquid Crystals* (London: Chapman & Hall)
[60] Kelly G, Mottram N J and Ramage A 2006 Electric field effects on nematic wetting layers *Mol. Cryst. Liq. Cryst.* **438** 271/[1835]–82/[1846]
[61] Chandrasekhar S 1992 *Liquid Crystals* (Cambridge: Cambridge University Press)
[62] Yin Y, Shiyanovskii S V, Golovin A B and Lavrentovich O D 2005 Dielectric torque and orientation dynamics of liquid crystals with dielectric dispersion *Phys. Rev. Lett.* **95** 087801
[63] Debye P J W 1929 *Polare Molekeln* (Leipzig: Hirzel Verlag)
[64] Hill N E, Vaughan W E, Price A H and Davies M 1969 *Dielectric Properties and Molecular Behaviour* (Princeton, NJ: Van Nostrand)